

Keypoint Cascade Voting for Point Cloud Based 6DoF Pose Estimation

Yangzheng Wu

Alireza Javaheri

Mohsen Zand

Michael Greenspan

RCVLab, Dept. of Electrical and Computer Engineering,
Queen's University, Kingston, Ontario, Canada

{ y.wu, javaheri.alireza, m.zand, greenspan.michael}@queensu.ca

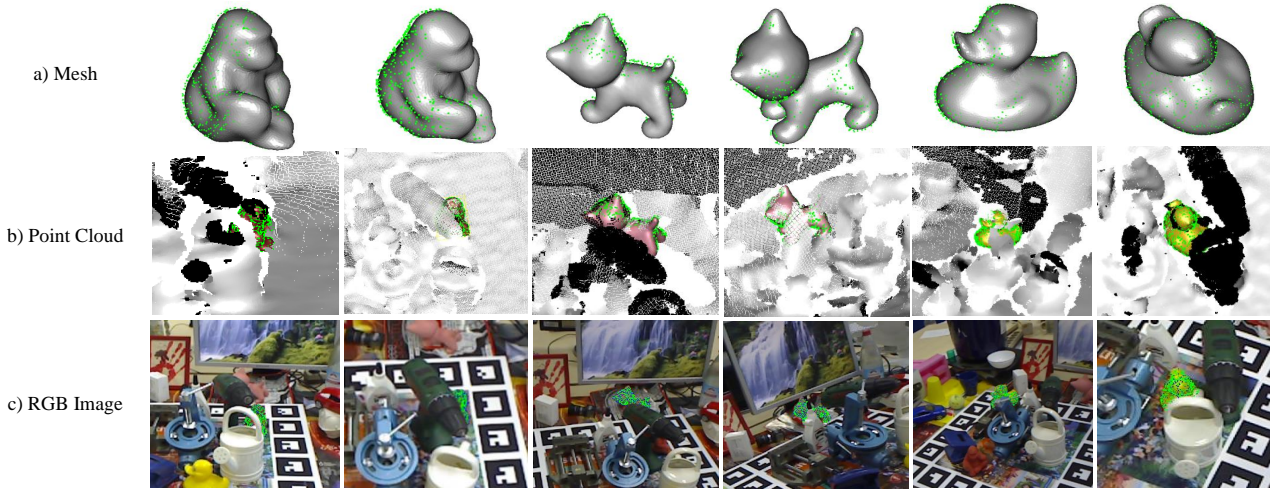


Figure 1: Samples of RCVPose3D results on Occlusion LINEMOD: The meshes are applied with groundtruth (GT) pose, the green points are applied with estimated poses, whereas the blue dots are projected GT poses. The color in Point Cloud and RGB images are for illustration only, as RGB data is not used for training or inference

Abstract

We propose a novel keypoint voting 6DoF object pose estimation method, which takes pure unordered point cloud geometry as input without RGB information. The proposed cascaded keypoint voting method, called RCVPose3D, is based upon a novel architecture which separates the task of semantic segmentation from that of keypoint regression, thereby increasing the effectiveness of both and improving the ultimate performance. The method also introduces a pairwise constraint in between different keypoints to the loss function when regressing the quantity for keypoint estimation, which is shown to be effective, as well as a novel Voter Confident Score which enhances both the learning and inference stages. Our proposed RCVPose3D achieves state-of-the-art performance on the Occlusion LINEMOD (74.5%) and YCB-Video (96.9%) datasets, outperforming existing pure RGB and RGB-D based methods, as well as being competitive with RGB plus point cloud methods.

1. Introduction

Accurate, robust and efficient six degree-of-freedom pose estimation (6DoF PE) is an enabling technology for applications such as augmented/virtual reality [21, 67], robotic grasping [32], autonomous driving [24], and so forth. 6DoF PE aims to determine the rigid transformation (comprising the 3DoF translation and 3DoF rotation) of an object of known geometry and/or appearance within a captured scene. This problem has been intensively investigated by the research community, initially using classical analytical approaches [1, 48, 36], and more recently exploiting the advent of machine learning (ML) methods [21, 67, 66, 13].

A number of recent leading ML approaches [42, 20, 66] have been proposed based on keypoint voting, in which the 3D scene coordinates of specific keypoints defined within an object's reference frame, are voted on and accumulated independently for each image pixel. The accuracy with which Convolutional Neural Networks (CNNs) are able to regress geometric information about the locations of key-

points within a scene is a main reason for the effectiveness of these approaches, and a number of variations have emerged which take both pure RGB [41, 55, 58, 68, 69, 28, 67, 62], as well as RGB-D [66, 50, 18, 20] data as input.

Whereas many classical approaches process 6DoF PE in 3D point clouds [48, 53, 36], the unordered nature of point clouds presents a challenge to ML approaches for which the ordering of the data matters. In particular, consecutive points in the points clouds may not be in the same neighborhood and due to the lack of proximity information, they cannot be fed to CNNs or in general Artificial Neural Network (ANN), unlike a pixel-ordered RGB or RGB-D image. Two approaches that have been proposed that impose order on the 3D data are voxel-based [18, 71, 37], in which the point cloud is cast to a 3D grid structure, and view-based, which resamples the data from a set of directions along the view sphere [21, 69, 22]. A further alternative has been to consider ML architectures that process point clouds independent of their ordering [3, 11, 15, 38, 35, 44, 51, 61]. The PointNet series [43, 45] has emerged as the most successful such approach, which makes use of a number of trainable symmetric functions which are invariant to point ordering.

In this work, we apply the powerful keypoint voting approach, taking pure 3D point cloud data as input. One challenge is a limitation to the size of the input point cloud. Whereas in processing conventional image-structured data (RGB, or RGB-D), the nature of CNNs can accommodate large input images, PointNet and other non-CNN based point cloud methods have a much stricter limit to the size of the input image. Further, in many realistic scenes, the object of interest comprises a relatively small percentage (e.g. 5%to15%) of the image [21, 67], so that the majority of the input data is considered background or clutter.

To address this, we have developed a novel keypoint voting architecture based on RCVPose [66] called RCV-Pose3D, which partitions the segmentation and regression tasks. In previous work, segmentation and regression were trained and executed in parallel, whereas in the proposed architecture, which we call *cascaded* keypoint voting, these tasks are trained independently and separately, and are executed end-to-end at inference. This novel architecture has two main benefits: First, training segmentation and regression separately increases the accuracy of each of these tasks, as they each have their own independent dedicated network. The second benefit is at inference, where background points are initially filtered out by the segmentation task, so that only foreground points are passed to regression. This not only reduces the computational expense of regression, but also increases voting effectiveness, as background points are filtered out. Some sample results are shown in Fig. 1.

The main contributions of this work are as follows:

- A novel cascade architecture for keypoint voting based 6DoF PE that partitions the segmentation and regres-

sion tasks. This improves training of these two independent tasks, and ultimately increases performance. Based on this architecture, we introduce RCVPose3D, which is the first variation of keypoint voting based 6DoF PE that takes pure 3D point cloud data as input.

- A novel loss function that considers the Euclidean distance between pairs of simultaneously regressed keypoints as a geometric constraint, and improves keypoint estimation accuracy.
- A novel evaluation score based on the voting space resolution. This score reduces the computational expense of training by evaluating the voter regression network, and culling certain points before voting, thereby accelerating hyperparameter tuning.

RCVPose3D has been thoroughly evaluated and compared against other state-of-the-art (SOTA) methods, and a series of ablation studies have been performed to characterize its effectiveness. The code is available to the public at <https://github.com/aaronWool/rcvpose3d>.

2. Related Work

This section reviews previous 6DoF PE work. Tab. 1 lists an overview of these works, classified by their input data modes of RGB, RGB-D, or 3D (i.e., point cloud).

2.1. 6DoF PE from RGB and RGB-D Images

Advances in 6DoF PE have been facilitated by the establishment of datasets such as LINEMOD [21] and YCB-Video [67], which include pose information of a variety of objects for a large number of RGB-D scenes under various cluttered and occluded conditions. The majority of ML-based methods have used pure RGB data images [55, 28, 41, 69, 58, 68, 62], while some have also used the depth (i.e. D) information provided by range sensors such as Microsoft Kinect [67, 18, 50]. For all RGB and RGB-D methods, the input images are multi-channel (i.e., 3- or 4-channel) 2D arrays with ordered pixel grids. These images are naturally handled by CNNs. OP-Net [30] is notable in that it processes only the D field of an RGB-D image, making use of the image ordering in a YOLO-like grid.

2.2. 6DoF PE from 3D Point Clouds

With the progress in the development and availability of 3D acquisition sensors, point clouds became popular in pose estimation [20, 19, 13, 18] and other computer vision applications [71]. Using a point cloud, surface and geometric constraints and characteristics of a rigid object are better exploited and can improve pose estimation in certain situations [20], such as in industrial applications where the

Method	Publication Date	Data Mode		
		RGB	D	3D
Tekin et al. [55]	2017	✓		
SSD-6D [28]	2017	✓		
Pix2Pose [41]	2019	✓		
DPOD [69]	2019	✓		
Trabelsi et al. [58]	2021	✓		
Dsc-posenet [68]	2021	✓		
GDR-Net [62]	2021	✓		
PoseCNN [67]	2017	✓	✓	
Tian et al. [57]	2020	✓	✓	
StablePose [50]	2021	✓	✓	
SO-Pose [8]	2021	✓	✓	
PVN3D [20]	2019	✓		✓
DenseFusion [60]	2019	✓		✓
PointVoteNet [18]	2020	✓		✓
FFB6D [19]	2021	✓		✓
RCVPose [66]	2021	✓	✓	✓
OP-Net [31]	2019		✓	
BaseNet [13]	2020			✓
RCVPose3D	2022			✓

Table 1: Methods with various input data modes

scanned parts are radiometrically textureless [32, 23]. Active range sensors, such as LiDaR, are also beneficial in applications such as autonomous driving [71, 49], where ambient lighting conditions can confound passive 2D sensors.

In some methods [20, 19, 60], the RGB data serves as the input to a CNN, and the 3D geometry data only enhances feature embedding. These methods have better performance compared to pure RGB methods, but they have never studied the impact of RGB and geometry separately. Geometry data has also been recently used by some RGB-D methods [69, 28, 67, 62] by applying pose refinement, such as ICP [2], as a post processing step.

Prior to the advent of ML in computer vision, many research works were dedicated to the design of effective 3D feature descriptors for 6DoF PE and many other applications. This includes a large variety of 3D feature descriptors such as Point Signatures [5], Spin Images [27], and Point Pair Features (PPF) [9]. For a thorough summary of classical 3D feature descriptors, see [17]. While the classical literature was replete with 6DoF PE solutions using point cloud data [16], there have been very few such ML-based works on 6DoF PE. An exception is BaseNet [13], which makes of use of PointNet for 3D feature extraction.

Following PointNet series [43, 45], several more recent ML methods designed for 3D point cloud/mesh were introduced. Point Transformer [70] adapts the transformer [59] to point clouds using vector attention. DGCNN [64] uses topology-based graph convolutions to extract 3D features. SubdivNet [25] investigate the properties of mesh and de-

sign a descriptor for it. Lastly, PPFNet [7] embeds the classic PPF into a CNN to encode features.

In addition to those methods that apply ICP for post-processing, there have been a few 6DoF PE methods that have made further use of 3D point cloud data. PVN3D [20] fuses PointNet features with 2D convolution features to estimate keypoints, the object center, and a semantic mask with a multi-task network loss all together. A least square fitting gives the final pose estimation. In PointVoteNet [18] the geometry and RGB information is voxelized and an anchor box is used to localize the target object location. The final pose is given by an offset clustering. While some recent works combine classic hand-crafted 3D descriptors such as PPF [7, 6] in the feature extraction stage. others use a topology graph [64, 34, 63] as a 3D feature descriptor instead of pure Euclidean local geometry.

3. Background: Keypoint Voting Framework

Classical voting methods such as Hough [10], RANSAC [12] Pose clustering [40] and Geometric Hashing [33] proved to be robust and highly effective. The accumulator space where all votes are aggregated independently, effectively filters out noise and background clutter, yielding an accurate estimation. With the advent of neural networks, voting techniques have gained more popularity. Recent works such as PVNet [42], PVN3D [20], and RCV-Pose [66] that exhibit leading SOTA performance, have merged voting-based methods, which are well established in the classical literature [61, 54], with recent ML-based keypoint estimation approaches.

The general keypoint voting architecture first proposed in PVNet for RGB input, and then modified in PVN3D and RCVPose for RGB-D input, is shown in Fig. 2a. We describe here the common elements and some variations of this architecture, and in Sec. 4 we introduce a number of modifications to accept as input unordered point cloud data.

The framework aims to estimate the 3D coordinates of a number of keypoints for an object in a scene. The keypoints themselves are simply a set of 3D points defined within the object-centric reference frame, and which therefore transform rigidly with the object. There is no requirement that all (or indeed even any) keypoints be visible in a scene, the main criterion being that there are at least 3 keypoints per object, and that they are sufficiently separated so as to allow for accurate recovery of the object pose. Keypoints have been defined in a variety of ways, including the object bounding box corners [39, 46, 56], farthest point sampling [42, 20], and disperse sampling [66].

As shown in Fig. 2a, the framework passes input image \mathcal{I} through an encoder-decoder network ED_{SM} . In PVNet, \mathcal{I} was an RGB image, and ED_{SM} was based on a ResNet-18 backbone. RCVPose used ResNet-152 for ED_{SM} for the RGB mode of an RGB-D input image \mathcal{I} , with D being

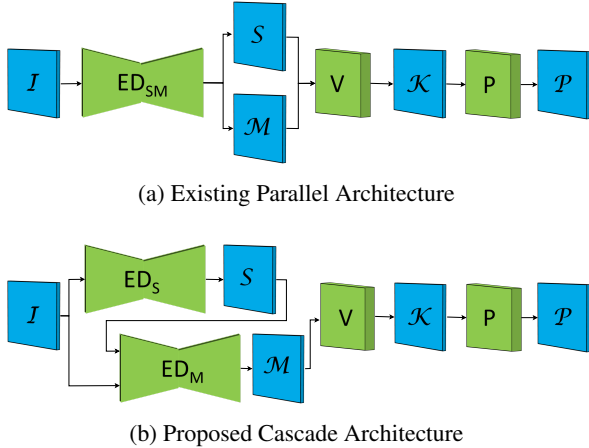


Figure 2: Existing parallel and proposed cascade keypoint voting architectures: I =input, ED_{SM} =combined segmentation/regression encoder-decoder, ED_S =segmentation encoder-decoder, ED_M =regression encoder-decoder, S =segmentation tensor, M =regression tensor, V =voting module, K =estimated keypoint coordinates, P =pose estimation module, \mathcal{P} =output estimated 6DoF object poses

used exclusively within the loss function and only during training. In PVN3D, \mathcal{I} was RGB-D, and there were two parallel encoder branches, with ResNet-34 applied to the RGB mode, and PointNet++ applied to the D mode. The output latent spaces from these two parallel branches were then fused and merged, and fed to the decoder stage.

The output of ED_{SM} are two tensors S and M , both of which have the same $W \times H$ spatial dimensions as input image \mathcal{I} . Segmentation mask S indicates to which (if any) object class each pixel belongs.

Tensor M contains the values of the regressed quantities for each pixel, that are aggregated to localize keypoints in the subsequent voting stage. In PVNet, M contains a set of 2D vectors for each pixel, that point in the direction of each keypoint. The subsequent voting module V integrates the intersections of all such vectors in a 2D accumulator space, the peaks of which indicate the locations of keypoints (i.e., *vector voting*). In PVN3D, M contains a set of 3D offsets, which translate the 3D coordinate of each pixel to vote for each keypoint within a 3D accumulator space (i.e., *offset voting*). In RCVPose, M contains a set of 1D values that indicate the Euclidean distance between each pixel and each keypoint. A set of spheres with radii equal to the values in M for each pixel, are rendered within a 3D accumulator space, and the peaks at intersections of the sphere surfaces determine the keypoint locations (i.e. *emphradial voting*).

The output of voting module V is tensor \mathcal{T} , comprising K estimated keypoints for each of the C objects. While segmentation provides a mechanism to handle multiple objects, in order to increase accuracy, in practice all of PVNet, PVN3D and RCVPose consider only a single object class

per network, i.e. $C = 1$. The $K \geq 3$ estimated keypoint scene coordinates, along with their corresponding canonical object-frame coordinates, are passed into pose module P to estimate the object 6DoF pose \mathcal{P} . For the purely 2D keypoint scene coordinates of PVNet, a RANSAC-based Perspective-n-Point (PnP) routine is used to recover the transformation, whereas for the 3D keypoint scene coordinates of PVN3D and RCVPose, a least squares fitting between two 3D point sets can be applied. Both PVN3D and RCVPose also refine the pose estimate further with a few ICP iterations, using a larger sample of 3D scene point data.

4. Proposed Cascade Approach: RCVPose3D

In this work, we propose a novel keypoint-based 6DoF PE method to estimate the pose of an object from pure point cloud data. The method regresses of the radius voting quantity of RCVPose [66], which has been recently proposed. The method combines three main aspects, the first of which is the separation of the semantic segmentation and pose estimation encoder-decoder networks, which are arranged in a cascade architecture (Sec. 4.1). The second is a novel loss function that considers the pairwise geometric constraints between simultaneously estimated keypoints (Sec. 4.3). The third aspect is a novel score function specific to voting methods, that facilitates training (Sec. 4.4). In the following subsections, we describe these aspects in detail.

4.1. Cascade Architecture

The proposed cascade architecture, shown in Fig. 2b, contains similar processing elements as the existing parallel architecture of Fig. 2a, albeit in a different arrangement. The main difference is that the segmentation and regression encoder-decoder network ED_{SM} of the parallel architecture, has been decoupled in the cascade architecture into two distinct networks, ED_S and ED_M . In cascade, the point cloud is first segmented prior to being passed to the regression stage. As shown in the figure, input point cloud I first passes through the (now independent) encoder-decoder network ED_S , which results in segmentation mask S . Only the filtered foreground points from S are then subsequently passed to regression network ED_M , resulting in tensor M which is then passed to the subsequent voting module V .

This new architecture has the advantage that each network ED_S and ED_M will learn their respective patterns independently, rather than training them jointly in a multitask fashion. This may seem counter-intuitive, as the essence of the popular multitask learning approach is to benefit from the interaction that occurs when training complementary tasks simultaneously. The key, however, is that multitask learning is mainly beneficial when the tasks contain correlated information that reinforces the learning process [65, 4, 52]. Our experiments (see Sec. 6.1) indicate that segmentation and keypoint regression are sufficiently

independent so that training them each independently significantly boosts the performance of each network, and ultimately the performance of pose estimation.

The other advantage of the cascade architecture is that it allows the regression network to be relatively lightweight (see Tab. 4), so that it is easier to train. Meanwhile, the estimation is typically more accurate compared to the regression existing in a parallel architecture. Last but not least, since it is a relatively small scale network, it will also not impact the time performance which is the initial reason most methods use parallel architecture initially.

One potential drawback of the cascade architecture is that it requires a larger memory footprint, to accommodate both networks. The regression network in particular is relatively lightweight, as only a small proportion ($\sim 5\%$ to 15%) of scene points need to be accommodated, so the memory footprint is in practice only $\sim 20\%$ larger than that of the parallel network (see Sec. 6.1).

4.2. 3D Feature Extraction Backend

In the proposed method shown in Fig. 2b, the encoder-decoder in the backend of both the segmentation network ED_S and the regression network ED_M , are accomplished with an effective 3D feature extractor. The unordered nature of 3D point cloud data poses a challenge to feature extraction, as the standard row column ordering that exists in 2D data and that is exploited by Convolutional Neural Networks is not present. To identify an appropriate 3D feature extractor, we implemented a number of learnable alternatives mentioned in Sec. 2.2 and results on shown in Sec. 6.2.

4.3. Radial Pair Loss \mathcal{L}_P

Existing methods calculate loss during training individually for each keypoint [42, 20, 66]. When multiple keypoints are estimated simultaneously, however, the potential exists to include a loss term that considers keypoint pairs.

Let k_i be a keypoint, with GT Euclidean distance $r_{mi} = \|p_m - k_i\|$ from object foreground point p_m . This is the radial distance that is learned and inferred by the regression network ED_M . It is invariant to rigid transformations, and therefore remains constant for changes in object pose.

Let $\hat{r}_{mi} = r_{mi} + \epsilon_{mi}$ be an estimate of this distance, with residual ϵ_{mi} . A *Residual Loss* term \mathcal{L}_ϵ that considers the residual values of only single keypoints can be formed as:

$$\mathcal{L}_\epsilon = \frac{1}{M \times K} \sum_{m=1}^M \sum_{i=1}^K SL_1(|\epsilon_{mi}|) \quad (1)$$

where $SL_1(\cdot)$ denotes the smooth L1 function, and which is summed for all M foreground points over all K keypoints.

An additional loss term is proposed here, which considers pairs of radial distances. Let $\Delta_{mij} = |r_{mi} - r_{mj}|$ be defined as the *radial pair difference*, which is the difference

between the GT radial values from a point p_m to keypoints k_i and k_j . Estimate $\hat{\Delta}_{mij}$ of Δ_{mij} is then formulated as:

$$\begin{aligned} \hat{\Delta}_{mij} &= |\hat{r}_{mi} - \hat{r}_{mj}| = |r_{mi} + \epsilon_{mi} - (r_{mj} + \epsilon_{mj})| \\ &\leq |r_{mi} - r_{mj}| + |\epsilon_{mi} - \epsilon_{mj}| \quad (2) \end{aligned}$$

This is an expression of the triangle inequality, which has been applied previously to improve efficiency in nearest neighbor search [14]. The radial pair difference is complementary to the magnitude of the residual used in the unary \mathcal{L}_ϵ loss. If \hat{r}_{mi} and \hat{r}_{mj} are both either underestimates or overestimates of their respective GT values (i.e. $\text{sign}(\epsilon_{mi}) = \text{sign}(\epsilon_{mj})$) then $|\epsilon_{mi} - \epsilon_{mj}| < \max(|\epsilon_{mi}|, |\epsilon_{mj}|)$, and the residual magnitude dominates. Alternately, if \hat{r}_{mi} and \hat{r}_{mj} fall on opposite sides of their respective GT values, then $\text{sign}(\epsilon_{mi}) = -\text{sign}(\epsilon_{mj})$, and $|\epsilon_{mi} - \epsilon_{mj}| \geq \max(|\epsilon_{mi}|, |\epsilon_{mj}|)$. In this case, the radial pair difference of Eq. 2 will exceed the residual magnitude.

We have exploited this by encapsulating Eq. 2 into the following loss term, which we call the *Radial Pair Loss*:

$$\mathcal{L}_P = \frac{2}{M \times K(K-1)} \sum_{m=1}^M \sum_{i=1}^K \sum_{j=i+1}^K SL_1(|\Delta_{mij} - \hat{\Delta}_{mij}|) \quad (3)$$

The \mathcal{L}_P can be used during the whole training process, but it can be delicate at the initial stage. The exact same residuals in between different radii for different keypoints can exist in the initial random output. It does become dominant at later epochs, when the regression network training to be closer to fully convergence (i.e. the outputs approach groundtruth (GT) radii values) by enforcing the constraint on inter-keypoints distances. Our experiments (see Sec. 6.4) supports this premise and shows the significant impact of \mathcal{L}_P on both accuracy and training time.

4.4. Voter Confidence Score

In the literature, two classic metrics have emerged and are commonly used to evaluate the overall performance on the 6DoF PE datasets: ADD(S) [21] for LMO, and ADD-S AUC [67] and ADD(S) AUC for YCB. We also introduce a new *Vote Confidence Score* (VCS) for the evaluation of the radii estimation, prior to the voting stage.

ADD(S) measures the average distance for asymmetric objects, and the minimum distance for symmetric objects, between points of the object transformed with GT pose and the object transformed with the estimated pose. If the distance is within 10% of the object diameter threshold, then the estimated pose is considered to be correct.

ADD(S) AUC is based on ADD(S). It creates a curve by plotting different thresholds against ADD(s) accuracy scores. The accuracy score of AUC is therefore given by the area underneath the curve.

ADD-S AUC is similar to ADD(S) AUC, except it uses ADD-S only for all objects, with the measurement based on minimum point distances.

Here we define **VCS** as a measure of each estimated voters’ confidence level from the regression network. VCS is formulated based on the voting space resolution. For a voting space resolution (e.g., edge length of a cubic voxel) of ρ , a vote is considered to be correct if the absolute error between the GT and estimated value is less than or equal to ρ . The confidence score is then the ratio of correct to total votes. This score can estimate the performance of the voting regression network, even before votes are cast in accumulator space, and can accelerate hyperparameter grid search. For radii voting specifically, VCS is defined as:

$$VCS = \frac{M'}{M} \quad (4)$$

where M is the number of votes and M' is the number of correct radii votes when $\epsilon_{m,i} = |r_{m,i} - \hat{r}_{m,i}| \leq \rho$. The voting space will apparently be more confident, with sharper peaks, when VCS is higher, and keypoint location will thus be more accurate (see Sec. 6.4).

5. Experiments

We evaluate the performance of our proposed RCV-Pose3D, and compare it with the best performing 6DoF PE methods on the two challenging 6DoF datasets that are commonly used in related SOTA work [42, 20].

5.1. Datasets

Occlusion LINEMOD [21] (LMO) is an extension of the LINEMOD dataset, comprising 1213 annotated RGB-D images of 9 classes of object, with GT pose and semantic labels. LMO is extremely challenging, not only because the objects within the scene are heavily occluded but also because it is purely for testing purposes, the convention being to train on the original LINEMOD dataset, which only comprises non-occluded objects.

YCB-Video (YCB), is a video-based 6DoF pose dataset, initially proposed by PoseCNN [67], which was the first CNN for 6DoF PE. YCB contains 130K frames extracted from 92 videos, with RGB images, depth maps, and GT poses and semantic masks provided for 21 classes of objects. The challenge of YCB is that some frames are blurred and include occluded objects. We follow previous works [42, 20, 66] and use a train/test split of 85%/15%.

5.2. Experimental Setup

To generate the 3D data, we use the camera intrinsic parameters to transform the depth maps into point clouds. Each point cloud is then downsampled to contain a total of $N = 2^{15}$ points, which is close to the limit that our GPU

could accommodate for a reasonable batch size of eight. Each point cloud is then recentered based on its bounding box, and normalized based on its maximum point value.

During training, the segmentation network inputs N points and estimates a semantic label for each point, indicating which object it falls on (if any). The segmentation output is randomly downsampled based on the estimated label probabilities, to comprise $M \leq 1024$ foreground points. The input of the regression network is the M foreground points, all of which have the same semantic label and thus fall on the surface of the object of interest. When training, these points are selected by applying the GT segmentation mask of the scene, and randomly downsampling the resulting foreground points to total M points.

At inference, the regression network estimates $j = 3$ keypoints’ radii simultaneously [66]. The output of the regression network is size $M \times 3$, comprising a radius from each input object point to all 3 keypoints.

The segmentation network’s loss function uses a standard Binary Cross Entropy (BCE) Loss \mathcal{L}_{bce} , whereas the regression network uses a combination of traditional Smooth L1 Loss on the radii residuals \mathcal{L}_ϵ (Eq. 1), and Radial Pair Loss \mathcal{L}_P (Eq. 3). The regression loss is then:

$$\mathcal{L}_r = \alpha \mathcal{L}_\epsilon + \beta \mathcal{L}_P \quad (5)$$

where α and β are weights that are adjusted during the training as follows: During the first 100 epochs, we set $\alpha = 0.8$ and $\beta = 0.2$ so that the network learns to approach the actual radii values with minor assistance from the radial pair constraint. For the remaining 150 epochs, α and β are adjusted to $\alpha = 0.2$, $\beta = 0.8$ for fine-tuning when \mathcal{L}_ϵ has mostly converged and \mathcal{L}_P dominates.

The Adam [29] optimizer is used for both networks during training. The initial learning rate is set to $1e^{-4}$ and reduces $\times 0.1$ for every 50 epochs. We train the networks with a batch size of 8 for segmentation and 32 for regression on three RTX6000 GPUs.

5.3. Performance Evaluation

To our knowledge, BaseNet [13] is the only other ML-based 6DoF PE method that inputs unordered point cloud data. OP-Net [32] does take pure depth data as input, although they use row-column image ordering using a YOLO-style [47] 2D grid decomposition, on a less common dataset. In addition to BaseNet, we also compare RCVPose3D with SOTA RGB and RGB-D methods. Two classic metrics are used to evaluate the overall performance of RCVPose3D, ADD(S) [21] for LMO, and ADD-S AUC [67] and ADD(S) AUC for YCB. Our experiments show that RCVPose3D is competitive with these other methods, even though it does not make use of any RGB information.

Mode	Method	Optional Refine?	YCB		LMO
			ADD(S) AUC	ADD-S AUC	ADD(s) [%]
RGB	Oberweger [39]	✗	72.8	-	27.1
	Hu et al. [26]	✗	-	-	30.4
	Pix2Pose [41]	✗	-	-	32.0
	DPOD [69]	✗	-	-	32.8
		✓	-	-	47.3
	PVNet [42]	✗	73.4	-	40.8
	PPRN [58]	✗	83.1	-	58.4
	SSD6D [28]	✓	-	-	27.5
	PoseCNN [67]	✗	59.9	75.8	24.9
		✓	85.4	93.0	-
GDR-Net [62]	✓	84.4	91.6	62.2	
SO-Pose [8]	✓	83.9	90.9	62.3	
RGB-D/ RGB+3D	Tian et al. [57]	✗	-	91.8	-
	RCVPose [66]	✗	95.2	96.6	70.2
		✓	<u>95.9</u>	97.2	71.1
	PVN3D [20]	✗	91.8	95.5	63.2
		✓	92.3	96.1	-
	FFB6D [19]	✗	92.7	<u>96.6</u>	66.2
	PointVoteNet [18]	✓	-	-	75.1
3D/Mesh	BaseNet [13]	✗	-	91.4	-
		✓	-	94.7	-
	RCVPose3D	✗	95.7	96.3	73.7
		✓	96.0	<u>96.6</u>	<u>74.5</u>

Table 2: LMO and YCB average accuracy results.

As shown in Tab. 2, on YCB, RCVPose3D performs better than all pure RGB methods. Its performance is especially relatively strong on objects such as *wood block* (+3% better) and *mug* (+1.7% better) which have a uniform color (see Supp. Mat.). RCVPose3D also outperforms all other SOTA methods with the relatively strict ADD(S) AUC metric, both with and without ICP refinement. It performs second best with the ADD-S AUC metric, approaching RCVPose [66] within a small margin (-0.6%).

On LMO, RCVPose3D again outperforms all SOTA methods that use RGB data. Similar to YCB, it estimates a better pose on objects with poor radiometric texture (almost uniform color) such as *eggbox* and *can*. It outperforms RCVPose by +3.4% for *can* (see Supp. Mat.). Compared to all methods, RCVPose3D is the second-best with on average only -0.6% less than PointVoteNet [18] which inputs both point cloud and RGB data (see Tab. 2).

Overall, RCVPose3D is the best performing metric for 6DoF PE on pure point cloud geometry. It also outperforms all methods that input pure RGB data. Finally, It is competitive with all other RGB-D/RGB+3D 6DoF PE methods, ranking either best or second best for different datasets and metrics.

6. Ablation Studies

We executed a series of experiments to characterize the benefits of the various novel elements of RCVPose3D using the common framework presented in Sec. 4. In particular, we characterized the impact of the cascade architecture and the Radial Pair Loss. We also compared the relative effectiveness of different backend 3D feature extractors. These

Architecture	mIoU		VCS		Loss
	train	test	train	test	
Parallel	85.6	63.2	54.5	52.1	\mathcal{L}_s
	91.2	<u>76.3</u>	63.5	<u>61.7</u>	$\mathcal{L}_r + \mathcal{L}_{bce}$
Cascade	100	91.7	95.4	93.7	$\mathcal{L}_r, \mathcal{L}_{bce}$

Table 3: Performance of segmentation for parallel vs. cascade architectures and varying losses, on LMO

Architecture	Loss	ICP	ADD(s)	memory	capacity	fps
Parallel (4SA)	\mathcal{L}_s	✗	49.9	20.4GB	1.88M	16
		✓	50.3			
	$\mathcal{L}_r + \mathcal{L}_{bce}$	✗	61.5			
		✓	61.9			
Parallel (6SA)	$\mathcal{L}_r + \mathcal{L}_{bce}$	✗	63.2	25.7GB	4.31M	15
		✓	63.7			
Cascade	$\mathcal{L}_r, \mathcal{L}_{bce}$	✗	<u>73.7</u>	25.1GB	3.76M	15
		✓	74.5			

Table 4: Pose estimation accuracy (ADD(s)) for parallel vs. cascade architectures and varying losses, on LMO

tests were all executed on the complete LMO dataset.

6.1. Parallel vs. Cascade, and Radial Pair Loss

A set of experiments were executed to isolate the impact of the cascade architecture on both the segmentation and regression stages, as well as the effect of Radial Pair Loss and the overall pose estimation accuracy.

For the cascade architecture, the configuration is as in Sec. 5.2. The parallel architecture takes the same input of $N = 2^{15}$ points. Its output, however, is $N \times 4$, which includes a semantic label and the 3 radii values to each of the corresponding keypoints for all N points. **Segmentation:** The first experiment investigates segmentation in isolation. The segmentation output (i.e. \mathcal{S} of Fig. 2a) is compared for both architectures by measuring mIoU against GT. As is the case with the cascade architecture, different loss functions are also applied to the parallel architectures. Initially, the Smooth L1 Loss \mathcal{L}_s is used to train both the segmentation and regression components, as in PVNet [42]. In order to compare with the cascade architecture fairly, the proposed Radial Pair Loss and BCE Loss are then applied afterwards.

The results are shown in Tab. 3. It can be seen that cascade significantly outperforms parallel, by over +15% in testing. Also, the Radial Pair Loss alone boosts performance of the parallel architecture by +13.1%.

Regression: A variation of the above experiment was repeated to evaluate regression in isolation. Here, the regression output (\mathcal{M} of Fig. 2a) is compared for both architectures and loss function combinations, by measuring VCS against GT. The results in Tab. 3 once again confirm that cascade outperforms parallel by +37%, and Radial Pair Loss boosts parallel performance by +9.6%.

It can be seen that cascade significantly outperforms parallel, by over +15% in testing. Radial Pair Loss alone boosts performance of the parallel architecture by +13.1%.

3D Descriptors	ICP	LMO	YCB	
		ADD(S)	ADD-S AUC	ADD(S) AUC
PointNet++ [45]	✗	73.7	96.3	95.7
	✓	74.5	96.6	96.0
Point Transformer [70]	✗	73.3	95.7	95.3
	✓	<u>73.8</u>	<u>96.0</u>	<u>95.6</u>
PPF+knn	✗	70.8	95.5	95.0
	✓	71.7	95.8	95.2
FPFH+knn	✗	70.6	94.6	93.2
	✓	71.3	94.9	93.6
DGCNN [64]	✗	70.1	92.8	90.9
	✓	70.7	93.0	91.1
SubdivNet [25]	✗	65.4	92.0	90.4
	✓	66.2	92.2	90.6

Table 5: Average accuracies of varied 3D descriptors

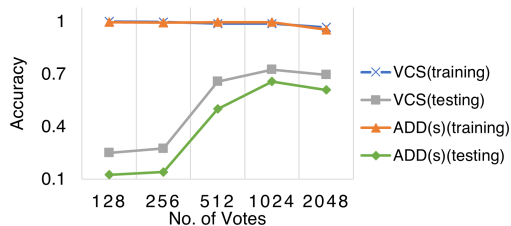


Figure 3: Impact of number of votes on accuracy (VCS and ADD(s)), tested on *ape* in LMO. The best is 1024 points

Pose Estimation: A further experiment evaluated the above combination of elements for the complete 6DoF PE pipeline, the results of which are shown in Tab. 4. The overall ADD(S) is boosted for cascade by +13% on average compared to parallel, with a small runtime sacrifice of 1 fps and a GPU memory cost of 4.7GB.

6.2. Comparison of Backend Feature Descriptors

There exist various backend networks in the literature, each encoding a distinct 3D feature descriptor. In order to find the most effective 3D feature descriptor, we compared the performance of RCVPose3D with different backend networks introduced in Sec. 4.2. The result in Tab. 5 show that PointNet++ [45] is the most accurate feature extractor, with Point Transformer [70] as a close second. PointNet was also more efficient, requiring only 1.8M parameters, with the next smallest being Point Transformers with 4.7M. We therefore used PointNet++ in the final RCVPose3D configuration, and for all other ablation experiments.

6.3. Impact of Number of Votes

In order to justify the number M of foreground points fed into the regression network, which in turn leads to M votes in the subsequent voting module, we trained the network with different numbers of votes forwarded through regression and into the accumulator space. Here we used the LMO *ape* object, and varied the number of votes over a range of from $M = 2^7$ to 2^{11} . The remaining hyperparam-

	\mathcal{L}_ϵ		$\mathcal{L}_r = \alpha\mathcal{L}_\epsilon + \beta\mathcal{L}_P$	
	$1e^{-3}$	$1e^{-4}$	$1e^{-3}$	$1e^{-4}$
initial learning rate	$1e^{-3}$	$1e^{-4}$	$1e^{-3}$	$1e^{-4}$
convergence time	5h	8h	3h	4h
VCS	45%	87%	<u>90%</u>	94%
ADD(s)	47.5	68.2	<u>73.2</u>	74.5

Table 6: Impact of Radial Pair Loss \mathcal{L}_P on radii regression. Parameters were fixed, except we reduced the batch size from 8 to 4 when $M = 2^{11}$, due to GPU memory limits.

Fig. 3 shows the accuracy for different number of votes using different metrics. The training VCS is consistently accurate and only drops slightly for 2^{11} votes. However, the testing VCS is significantly worse when there are fewer points. ADD(S) also shows a similar trend. Both VCS and ADD(S) slightly decrease when the number of votes is larger than 2^{10} . This is most likely due to the smaller batch size for 2^{11} votes. We ended up using $M = 2^{10}$ votes for optimal performance.

6.4. Impact of Radial Pair Loss \mathcal{L}_P

In order to show the impact of the proposed \mathcal{L}_P , we trained a radii regression network with the same configuration in Sec. 5.2 but using \mathcal{L}_ϵ , and compared it with the combined $\mathcal{L}_\epsilon + \mathcal{L}_P$ loss. We then use VCS, the newly proposed score proved to be consistent with ADD(S) in Sec. 3 and Sec. 6.1, to evaluate the regression performance. As shown in Tab. 6, the network supervised by \mathcal{L}_P is not only more accurate, but it also converges faster. Performance actually doubles for learning rate $1e-3$ in which the network does not perform well using \mathcal{L}_ϵ .

7. Conclusion

We propose a novel cascade architecture for 6 DoF PE from pure point cloud data, i.e. without RGB information. PointNet++ [45] is selected for the segmentation and regression backbones, after carefully considering different 3D feature extractors. A novel radial pair loss function (\mathcal{L}_P) is proposed and shown to further improve the performance. Finally, a novel score, Vote Count Score (VCS), for the accuracy of the regression network voting technique (VCS) is proposed and shown to improve training. We achieve competitive results on two popular datasets, LMO and YCB, where RCVPose3D outperforms the SOTA methods that use pure RGB information. When compared to methods that input RGB-D and RGB + point cloud data, RCVPose3D is the best performing method in YCB with the ADD(S) AUC metric. It is also the second best for other combinations of datasets and metrics. Lastly, our time performance is 15 fps, which is competitive with other SOTA methods.

Acknowledgements: This work was supported by Bluewrist Inc. and NSERC.

References

- [1] Aitor Aldoma, Markus Vincze, Nico Blodow, David Gossow, Suat Gedikli, Radu Bogdan Rusu, and Gary Bradski. Cad-model recognition and 6dof pose estimation using 3d cues. In *2011 IEEE international conference on computer vision workshops (ICCV workshops)*, pages 585–592. IEEE, 2011. [1](#)
- [2] P.J. Besl and Neil D. McKay. A method for registration of 3-d shapes. *IEEE Transactions on Pattern Analysis and Machine Intelligence*, 14(2):239–256, 1992. [3](#)
- [3] Joan Bruna, Wojciech Zaremba, Arthur Szlam, and Yann LeCun. Spectral networks and locally connected networks on graphs. *arXiv preprint arXiv:1312.6203*, 2013. [2](#)
- [4] Zhe Cao, Tomas Simon, Shih-En Wei, and Yaser Sheikh. Realtime multi-person 2d pose estimation using part affinity fields. In *Proceedings of the IEEE conference on computer vision and pattern recognition*, pages 7291–7299, 2017. [4](#)
- [5] Chin Seng Chua and Ray Jarvis. Point signatures: A new representation for 3d object recognition. *International Journal of Computer Vision*, 25(1):63–85, 1997. [3](#)
- [6] Haowen Deng, Tolga Birdal, and Slobodan Ilic. Ppf-foldnet: Unsupervised learning of rotation invariant 3d local descriptors. In *Proceedings of the European Conference on Computer Vision (ECCV)*, pages 602–618, 2018. [3](#)
- [7] Haowen Deng, Tolga Birdal, and Slobodan Ilic. Ppfnet: Global context aware local features for robust 3d point matching. In *Proceedings of the IEEE conference on computer vision and pattern recognition*, pages 195–205, 2018. [3](#)
- [8] Yan Di, Fabian Manhardt, Gu Wang, Xiangyang Ji, Nassir Navab, and Federico Tombari. So-pose: Exploiting self-occlusion for direct 6d pose estimation. In *Proceedings of the IEEE/CVF International Conference on Computer Vision (ICCV)*, pages 12396–12405, October 2021. [3, 7](#)
- [9] Bertram Drost, Markus Ulrich, Nassir Navab, and Slobodan Ilic. Model globally, match locally: Efficient and robust 3d object recognition. In *2010 IEEE computer society conference on computer vision and pattern recognition*, pages 998–1005. Ieee, 2010. [3](#)
- [10] Richard O Duda and Peter E Hart. Use of the hough transformation to detect lines and curves in pictures. *Communications of the ACM*, 15(1):11–15, 1972. [3](#)
- [11] Yi Fang, Jin Xie, Guoxian Dai, Meng Wang, Fan Zhu, Tiantian Xu, and Edward Wong. 3d deep shape descriptor. In *Proceedings of the IEEE Conference on Computer Vision and Pattern Recognition*, pages 2319–2328, 2015. [2](#)
- [12] Martin A Fischler and Robert C Bolles. Random sample consensus: a paradigm for model fitting with applications to image analysis and automated cartography. *Communications of the ACM*, 24(6):381–395, 1981. [3](#)
- [13] Ge Gao, Mikko Lauri, Yulong Wang, Xiaolin Hu, Jianwei Zhang, and Simone Frntrop. 6d object pose regression via supervised learning on point clouds. In *2020 IEEE International Conference on Robotics and Automation (ICRA)*, pages 3643–3649. IEEE, 2020. [1, 2, 3, 6, 7](#)
- [14] M. Greenspan and G. Godin. A nearest neighbor method for efficient icp. In *Proceedings Third International Conference on 3-D Digital Imaging and Modeling*, pages 161–168, 2001. [5](#)
- [15] Kan Guo, Dongqing Zou, and Xiaowu Chen. 3d mesh labeling via deep convolutional neural networks. *ACM Transactions on Graphics (TOG)*, 35(1):1–12, 2015. [2](#)
- [16] Yulan Guo, Mohammed Bennamoun, Ferdous Sohel, Min Lu, and Jianwei Wan. 3d object recognition in cluttered scenes with local surface features: A survey. *IEEE Transactions on Pattern Analysis and Machine Intelligence*, 36(11):2270–2287, 2014. [3](#)
- [17] Yulan Guo, Mohammed Bennamoun, Ferdous Sohel, Min Lu, Jianwei Wan, and Ngai Ming Kwok. A comprehensive performance evaluation of 3d local feature descriptors. *International Journal of Computer Vision*, 116(1):66–89, 2016. [3](#)
- [18] Frederik Hagelskjær and Anders Glent Buch. Pointvotenet: Accurate object detection and 6 dof pose estimation in point clouds. In *2020 IEEE International Conference on Image Processing (ICIP)*, pages 2641–2645. IEEE, 2020. [2, 3, 7](#)
- [19] Yisheng He, Haibin Huang, Haoqiang Fan, Qifeng Chen, and Jian Sun. Ffb6d: A full flow bidirectional fusion network for 6d pose estimation. In *Proceedings of the IEEE/CVF Conference on Computer Vision and Pattern Recognition*, pages 3003–3013, 2021. [2, 3, 7](#)
- [20] Yisheng He, Wei Sun, Haibin Huang, Jianran Liu, Haoqiang Fan, and Jian Sun. Pvn3d: A deep point-wise 3d keypoints voting network for 6dof pose estimation. In *Proceedings of the IEEE/CVF Conference on Computer Vision and Pattern Recognition (CVPR)*, June 2020. [1, 2, 3, 5, 6, 7](#)
- [21] Stefan Hinterstoisser, Vincent Lepetit, Slobodan Ilic, Stefan Holzer, Gary Bradski, Kurt Konolige, and Nassir Navab. Model based training, detection and pose estimation of texture-less 3d objects in heavily cluttered scenes. In *Asian conference on computer vision*, pages 548–562. Springer, 2012. [1, 2, 5, 6](#)
- [22] Tomas Hodan, Daniel Barath, and Jiri Matas. Epos: Estimating 6d pose of objects with symmetries. In *Proceedings of the IEEE/CVF conference on computer vision and pattern recognition*, pages 11703–11712, 2020. [2](#)
- [23] Tomáš Hodaň, Pavel Haluza, Štěpán Obržálek, Jiří Matas, Manolis Lourakis, and Xenophon Zabulis. T-LESS: An RGB-D dataset for 6D pose estimation of texture-less objects. *IEEE Winter Conference on Applications of Computer Vision (WACV)*, 2017. [3](#)
- [24] Jordan SK Hu, Tianshu Kuai, and Steven L Waslander. Point density-aware voxels for lidar 3d object detection. *arXiv preprint arXiv:2203.05662*, 2022. [1](#)
- [25] Shi-Min Hu, Zheng-Ning Liu, Meng-Hao Guo, Jun-Xiong Cai, Jiahui Huang, Tai-Jiang Mu, and Ralph R Martin. Subdivision-based mesh convolution networks. *arXiv preprint arXiv:2106.02285*, 2021. [3, 8](#)
- [26] Yinlin Hu, Joachim Hugonot, Pascal Fua, and Mathieu Salzmann. Segmentation-driven 6d object pose estimation. In *Proceedings of the IEEE/CVF Conference on Computer Vision and Pattern Recognition*, pages 3385–3394, 2019. [7](#)
- [27] Jihad H’roua, Michaël Roy, Alamin Mansouri, Driss Mammas, Patrick Juillion, Ali Bouzit, and Patrice Méniel. Salient spin images: A descriptor for 3d object recognition.

- In *International conference on image and signal processing*, pages 233–242. Springer, 2018. 3
- [28] Wadim Kehl, Fabian Manhardt, Federico Tombari, Slobodan Ilic, and Nassir Navab. Ssd-6d: Making rgb-based 3d detection and 6d pose estimation great again. In *Proceedings of the IEEE international conference on computer vision*, pages 1521–1529, 2017. 2, 3, 7
- [29] Diederik P. Kingma and Jimmy Ba. Adam: A method for stochastic optimization. In Yoshua Bengio and Yann LeCun, editors, *3rd International Conference on Learning Representations, ICLR 2015, San Diego, CA, USA, May 7-9, 2015, Conference Track Proceedings*, 2015. 6
- [30] Kilian Kleeberger and Marco F Huber. Single shot 6d object pose estimation. In *2020 IEEE International Conference on Robotics and Automation (ICRA)*, pages 6239–6245. IEEE, 2020. 2
- [31] Kilian Kleeberger and Marco F. Huber. Single shot 6d object pose estimation. In *2020 IEEE International Conference on Robotics and Automation (ICRA)*, pages 6239–6245, 2020. 3
- [32] Kilian Kleeberger, Christian Landgraf, and Marco F Huber. Large-scale 6d object pose estimation dataset for industrial bin-picking. In *2019 IEEE/RSJ International Conference on Intelligent Robots and Systems (IROS)*, pages 2573–2578. IEEE, 2019. 1, 3, 6
- [33] Y. Lamdan and H. J. Wolfson. Geometric hashing: A general and efficient model-based recognition scheme. In *[1988 Proceedings] Second International Conference on Computer Vision*, pages 238–249, 1988. 3
- [34] Yangyan Li, Rui Bu, Mingchao Sun, Wei Wu, Xinhan Di, and Baoquan Chen. Pointcnn: Convolution on x-transformed points. *Advances in neural information processing systems*, 31:820–830, 2018. 3
- [35] Yangyan Li, Soeren Pirk, Hao Su, Charles R Qi, and Leonidas J Guibas. Fpnn: Field probing neural networks for 3d data. *Advances in Neural Information Processing Systems*, 29:307–315, 2016. 2
- [36] Yunpeng Li, Noah Snavely, Dan Huttenlocher, and Pascal Fua. Worldwide pose estimation using 3d point clouds. In *European conference on computer vision*, pages 15–29. Springer, 2012. 1, 2
- [37] Zhijian Liu, Haotian Tang, Yujun Lin, and Song Han. Point-voxel cnn for efficient 3d deep learning. *Advances in Neural Information Processing Systems*, 32, 2019. 2
- [38] Jonathan Masci, Davide Boscaini, Michael Bronstein, and Pierre Vandergheynst. Geodesic convolutional neural networks on riemannian manifolds. In *Proceedings of the IEEE international conference on computer vision workshops*, pages 37–45, 2015. 2
- [39] Markus Oberweger, Mahdi Rad, and Vincent Lepetit. Making deep heatmaps robust to partial occlusions for 3d object pose estimation. In *Proceedings of the European Conference on Computer Vision (ECCV)*, pages 119–134, 2018. 3, 7
- [40] Clark F. Olson. Efficient pose clustering using a randomized algorithm, 1997. 3
- [41] Kiru Park, Timothy Patten, and Markus Vincze. Pix2pose: Pixel-wise coordinate regression of objects for 6d pose estimation. In *Proceedings of the IEEE/CVF International Conference on Computer Vision*, pages 7668–7677, 2019. 2, 3, 7
- [42] Sida Peng, Yuan Liu, Qixing Huang, Xiaowei Zhou, and Hujun Bao. Pvnnet: Pixel-wise voting network for 6dof pose estimation. In *Proceedings of the IEEE/CVF Conference on Computer Vision and Pattern Recognition*, pages 4561–4570, 2019. 1, 3, 5, 6, 7
- [43] Charles R Qi, Hao Su, Kaichun Mo, and Leonidas J Guibas. Pointnet: Deep learning on point sets for 3d classification and segmentation. In *Proceedings of the IEEE conference on computer vision and pattern recognition*, pages 652–660, 2017. 2, 3
- [44] Charles R Qi, Hao Su, Matthias Nießner, Angela Dai, Mengyuan Yan, and Leonidas J Guibas. Volumetric and multi-view cnns for object classification on 3d data. In *Proceedings of the IEEE conference on computer vision and pattern recognition*, pages 5648–5656, 2016. 2
- [45] Charles R Qi, Li Yi, Hao Su, and Leonidas J Guibas. Pointnet++: Deep hierarchical feature learning on point sets in a metric space. *arXiv preprint arXiv:1706.02413*, 2017. 2, 3, 8
- [46] Mahdi Rad and Vincent Lepetit. Bb8: A scalable, accurate, robust to partial occlusion method for predicting the 3d poses of challenging objects without using depth. In *Proceedings of the IEEE International Conference on Computer Vision*, pages 3828–3836, 2017. 3
- [47] Joseph Redmon and Ali Farhadi. Yolo9000: better, faster, stronger. In *Proceedings of the IEEE conference on computer vision and pattern recognition*, pages 7263–7271, 2017. 6
- [48] Radu Bogdan Rusu, Gary Bradski, Romain Thibaux, and John Hsu. Fast 3d recognition and pose using the viewpoint feature histogram. In *2010 IEEE/RSJ International Conference on Intelligent Robots and Systems*, pages 2155–2162. IEEE, 2010. 1, 2
- [49] Weijing Shi and Raj Rajkumar. Point-gnn: Graph neural network for 3d object detection in a point cloud. In *Proceedings of the IEEE/CVF conference on computer vision and pattern recognition*, pages 1711–1719, 2020. 3
- [50] Yifei Shi, Junwen Huang, Xin Xu, Yifan Zhang, and Kai Xu. Stablepose: Learning 6d object poses from geometrically stable patches. In *Proceedings of the IEEE/CVF Conference on Computer Vision and Pattern Recognition*, pages 15222–15231, 2021. 2, 3
- [51] Hang Su, Subhransu Maji, Evangelos Kalogerakis, and Erik Learned-Miller. Multi-view convolutional neural networks for 3d shape recognition. In *Proceedings of the IEEE international conference on computer vision*, pages 945–953, 2015. 2
- [52] Ximeng Sun, Rameswar Panda, Rogerio Feris, and Kate Saenko. Adashare: Learning what to share for efficient deep multi-task learning. *Advances in Neural Information Processing Systems*, 33:8728–8740, 2020. 4
- [53] Babak Taati and Michael Greenspan. Local shape descriptor selection for object recognition in range data. *Computer Vision and Image Understanding*, 115(5):681–694, 2011. Special issue on 3D Imaging and Modelling. 2
- [54] Alykhan Tejani, Danhang Tang, Rigas Kouskouridas, and Tae-Kyun Kim. Latent-class hough forests for 3d object

- detection and pose estimation. In *European Conference on Computer Vision*, pages 462–477. Springer, 2014. 3
- [55] Bugra Tekin, Sudipta N Sinha, and Pascal Fua. Real-time seamless single shot 6d object pose prediction. In *Proceedings of the IEEE Conference on Computer Vision and Pattern Recognition*, pages 292–301, 2018. 2, 3
- [56] Bugra Tekin, Sudipta N Sinha, and Pascal Fua. Real-time seamless single shot 6d object pose prediction. In *Proceedings of the IEEE conference on computer vision and pattern recognition*, pages 292–301, 2018. 3
- [57] Meng Tian, Liang Pan, Marcelo H Ang, and Gim Hee Lee. Robust 6d object pose estimation by learning rgb-d features. In *2020 IEEE International Conference on Robotics and Automation (ICRA)*, pages 6218–6224, 2020. 3, 7
- [58] Ameni Trabelsi, Mohamed Chaabane, Nathaniel Blanchard, and Ross Beveridge. A pose proposal and refinement network for better 6d object pose estimation. In *Proceedings of the IEEE/CVF Winter Conference on Applications of Computer Vision*, pages 2382–2391, 2021. 2, 3, 7
- [59] Ashish Vaswani, Noam Shazeer, Niki Parmar, Jakob Uszkoreit, Llion Jones, Aidan N Gomez, Łukasz Kaiser, and Illia Polosukhin. Attention is all you need. *Advances in neural information processing systems*, 30, 2017. 3
- [60] Chen Wang, Danfei Xu, Yuke Zhu, Roberto Martín-Martín, Cewu Lu, Li Fei-Fei, and Silvio Savarese. Densefusion: 6d object pose estimation by iterative dense fusion. In *Proceedings of the IEEE/CVF Conference on Computer Vision and Pattern Recognition*, pages 3343–3352, 2019. 3
- [61] Dominic Zeng Wang and Ingmar Posner. Voting for voting in online point cloud object detection. In *Robotics: Science and Systems*, volume 1, pages 10–15. Rome, Italy, 2015. 2, 3
- [62] Gu Wang, Fabian Manhardt, Federico Tombari, and Xiangyang Ji. Gdr-net: Geometry-guided direct regression network for monocular 6d object pose estimation. In *Proceedings of the IEEE/CVF Conference on Computer Vision and Pattern Recognition*, pages 16611–16621, 2021. 2, 3, 7
- [63] Peng-Shuai Wang, Yang Liu, Yu-Xiao Guo, Chun-Yu Sun, and Xin Tong. O-cnn: Octree-based convolutional neural networks for 3d shape analysis. *ACM Transactions On Graphics (TOG)*, 36(4):1–11, 2017. 3
- [64] Yue Wang, Yongbin Sun, Ziwei Liu, Sanjay E Sarma, Michael M Bronstein, and Justin M Solomon. Dynamic graph cnn for learning on point clouds. *Acm Transactions On Graphics (tog)*, 38(5):1–12, 2019. 3, 8
- [65] Dong Wu, Manwen Liao, Weitian Zhang, and Xinggang Wang. Yolop: You only look once for panoptic driving perception. *arXiv preprint arXiv:2108.11250*, 2021. 4
- [66] Yangzheng Wu, Mohsen Zand, Ali Etemad, and Michael Greenspan. Vote from the center: 6 dof pose estimation in rgb-d images by radial keypoint voting. *arXiv preprint arXiv:2104.02527*, 2021. 1, 2, 3, 4, 5, 6, 7
- [67] Yu Xiang, Tanner Schmidt, Venkatraman Narayanan, and Dieter Fox. Posecnn: A convolutional neural network for 6d object pose estimation in cluttered scenes. 2018. 1, 2, 3, 5, 6, 7
- [68] Zongxin Yang, Xin Yu, and Yi Yang. Dsc-posenet: Learning 6dof object pose estimation via dual-scale consistency. In *Proceedings of the IEEE/CVF Conference on Computer Vision and Pattern Recognition*, pages 3907–3916, 2021. 2, 3
- [69] Sergey Zakharov, Ivan Shugurov, and Slobodan Ilic. Dpod: 6d pose object detector and refiner. In *Proceedings of the IEEE/CVF International Conference on Computer Vision*, pages 1941–1950, 2019. 2, 3, 7
- [70] Hengshuang Zhao, Li Jiang, Jiaya Jia, Philip HS Torr, and Vladlen Koltun. Point transformer. In *Proceedings of the IEEE/CVF International Conference on Computer Vision*, pages 16259–16268, 2021. 3, 8
- [71] Yin Zhou and Oncel Tuzel. Voxnet: End-to-end learning for point cloud based 3d object detection. In *Proceedings of the IEEE conference on computer vision and pattern recognition*, pages 4490–4499, 2018. 2, 3

Supplementary Material: Keypoint Cascade Voting for Point Cloud Based 6DoF Pose Estimation

Yangzheng Wu

Alireza Javaheri

Mohsen Zand

Michael Greenspan

Dept. of Electrical and Computer Engineering, Ingenuity Labs Research Institute
Queen’s University, Kingston, Ontario, Canada

{ y.wu, javaheri.alireza, m.zand, greenspan.michael}@queensu.ca

S.1. Overview

Here we show additional experiments and their associated results. First, the accuracy of RCVPose3D for each individual object is compared with other methods in Sec. S.2 as well as samples for all LMO objects in Fig. S.1. In Sec. S.3, more experimental results are provided to support our decision on choosing PointNet++ as the backend feature extractor in RCVPose3D. We report detailed results in Tab. S.5 and Tab. S.3, with time performance listed in Tab. S.1.

S.2. Accuracy Results per Object

In Sec. 5.3 of the main paper, we have claimed that the performance of RCVPose3D is relatively strong on objects with uniform colors, such as *wood block* and *mug* in YCB. The performance gains for these objects are respectively 3% and 1.7%. In Tab. S.4, AUC and ADD(s) results of different methods are listed for all the objects in the YCB dataset. A similar statement was made for *eggbox* and *can* on LMO. Tab. S.2 shows that RCVPose3D outperforms other methods by 3.4% for *can*, and hence, it is the second best by only 0.6% lower ADD(s) for *eggbox*.

S.3. Best 3D Feature Extractor

In order to identify the best 3D feature extractor for RCVPose3D, we implemented and/or tested a number of learnable feature extractors including PointNet++ [S.14], Point Transformer [S.23], DGCNN [S.19], SubdivNet [S.8], and L-PPF & L-FPFH.

1) **PointNet++** [S.14] constructs a series of feature vectors with a Set Abstraction (SA) Module, which groups the points and encodes local geometry into learnable features. We used three Set Abstraction layers. Farthest Point Sampling is used to partition the point cloud into a set of clusters, which covers the entire point cloud. It samples cluster centers and ensures the points are sparse to avoid overlap-

ping between the clusters. It therefore results in sampling the entire point cloud properly. We set two levels of scales in Multi-Scale Grouping (MSG) of each Set Abstraction Layer. A series of 2D convolution layers with batch normalization and max pooling are applied on the grouped points feature vector to generate a convolutional feature vector associated with each cluster center. The PointNet++ descriptor creates four different hierarchy clusters which encode both local and global geometries. It is also called Vanilla since it is the most original design of Pointnet series.

2) **Point Transformer** [S.23] is an extended version of Transformers performed on Natural Language Processing (NLP) and visual processing tasks. Leaving out the unordered nature of point clouds, point cloud structure is very similar to linguistic data, in that the self attention mechanism still applies to point clouds when encoding features from different positions.

According to [S.23], there are two types of attention in literature, i.e. *scalar* and *vector*. Vector attention is more accurate since it adapts itself to all feature channels separately and not to the whole feature vectors as in scalar attention [S.23]. We used the semantic segmentation structure of the Point Transformer to segment the point cloud in our architecture. The regression part is also modified accordingly in order to produce pointwise radii estimation.

3) **DGCNN** [S.19] encodes the feature descriptor by using a k-nearest neighbor (KNN) approach. For each point in the input point cloud of size $N \times 3$, DGCNN finds the $k = 20$ nearest neighbor points and concatenates indices of those points together to encode the topological graph of the local region. Then a 2D convolution is applied to the graph and encodes it into feature vectors. This process is repeated multiple times during the feature extraction stage. DGCNN is a topology graph-based encoder that encodes only local features.

4) **Subdivnet** [S.8] is a network designed for encoding triangle meshes by simulating a 2D image convolution. The

convolution kernel operates on a neighborhood of four manifold triangles. The triangle e at the center is the kernel of a set of neighboring triangles, denoted as e_0, e_1, \dots, e_{K-1} . The mesh convolution kernel is defined by a linear combination of four elements, i.e., the center feature, the sum of neighbors, the differential sum in between neighbors, and the differential sum in between neighbors and the center. It is formulated as:

$$\begin{aligned} Conv(f) = & w_0 e + w_1 \sum_{i=0}^{K-1} e_i + \\ & w_2 \sum_{i=0}^{K-2} |e_{i+1} - e_i| + \\ & w_3 \sum_{i=0}^{K-1} |e - e_i| \end{aligned} \quad (\text{S.1})$$

where w_0, w_1, w_2, w_3 are trainable weights. We use a kernel size of 3, so that the sum is from the three neighbors of the center mesh. The features are extracted by mesh convolutions and encoded to be similar to an 2D image.

5) L-PPF & L-FPFH is inspired by PPFNet [S.1] and DGCNN [S.19], and uses a K-Nearest Neighbor (KNN) approach to encode local neighborhoods. Two classic feature descriptors, FPFH[S.15] and PPF[S.2], are interpolated with learnable weights to assist the encoder of the network. The encoder contains multiple hybrid convolutional blocks. Each block contains three layers in general. The first layer takes pure point cloud as input. Then, the Farthest Point Sampling selects the cluster centers p_i . For each p_i , k nearest neighbors are selected. Since k nearest points are forced to be selected, it is robust to uneven point distribution on the surface of the object. We concatenate these hand-crafted descriptors to the network. Farthest Point Sampling is used to sample the input $N \times 3$ points into M clusters centered at $P^c = \{p_i^c | i = 0, 1 \dots M\}$ $P^c = \{p_i^c\}_{i=1}^M$ initially within each block. Then the K nearest neighbor points $P^k = \{p_i^k | i = 0, 1 \dots K\}$ $P^k = \{p_i^k\}_{i=1}^K$ within a certain range of d of the cluster centers are selected to compute the classic descriptor. PPF is based on the point pairs in between each cluster center $p_i^c \in P^c$ and those points $p_i^k \in P^k$ among them. Similarly, FPFH is encoded based on all points $p_i^k \in P^k$ within each of the clusters $p_i^c \in P^c$. The $k \times f$ classical descriptor vector (in the L-PPF scenario, $f=4$) is then flattened and stacked into a $m \times (k \times f)$ classical feature vector. To make it learnable, a 1D convolution with a kernel size of f is applied to this feature vector. The exact same operations are duplicated multiple times, and each time the cluster centers are sampled based on the previous layers' centers. In this way, features at different hierarchies are encoded into the network.

These descriptors are further adjusted to fit as the feature extraction backend in the RCVPose3D architecture. All descriptors are trained with the identical hyperparameter configurations mentioned in Sec. 5.2. It was shown in Sec. 6.2

of the main paper that PointNet++ [S.14] and Point Transformer [S.23] are the most accurate 3D feature descriptors compared to the other alternatives. Tab. S.3 and Tab. S.5 contain the same results per object. PointNet++ is also the fastest (w.r.t. training) and the most memory efficient feature descriptor. It converges in 16h and requires only 1.8M parameters, compared to 22h convergence time and 4.7M parameters of the Point Transformers in the second place, as shown in Tab. S.1.

3D Descriptor	Time	# Parameters
PointNet++	16h	1.8M
Point Transformer [S.23]	22h	4.7M
PPF+knn	48h	9.7M
FPFH+knn	48h	9.8M
DGCNN [S.19]	70h	10.2M
SubdivNet [S.8]	65h	5.8M

Table S.1. Training time and number of trainable parameters comparison of different 3D feature descriptors

Mode	Method	Object								Mean	
		ape	can	cat	driller	duck	eggbox*	glue*	hole-puncher		
RGB	Oberweger [S.11]	12.1	39.9	8.2	45.2	17.2	22.1	35.8	36.0	27.1	
	Hu et al. [S.9]	17.6	53.9	3.3	62.4	19.2	25.9	39.6	21.3	30.4	
	Pix2Pose [S.12]	22.0	44.7	22.7	44.7	15.0	25.2	32.4	49.5	32.0	
	DPOD [S.22]	-	-	-	-	-	-	-	-	-	32.8
	PVNet [S.13]	15.8	63.3	16.7	25.2	65.7	50.2	49.6	39.7	40.8	
	PPRN [S.17]	-	-	-	-	-	-	-	-	-	58.4
RGB +D ref	YOLO6D [S.16]	-	-	-	-	-	-	-	-	6.4	
	SSD6D+ref [S.10]	-	-	-	-	-	-	-	-	27.5	
	PoseCNN [S.21]	9.6	45.2	0.9	41.4	19.6	22.0	38.5	22.1	24.9	
	DPOD+ref [S.22]	-	-	-	-	-	-	-	-	47.3	
RGB-D/RGB+3D	RCVPose	60.3	92.5	50.2	78.2	52.1	81.2	72.1	75.2	70.2	
	RCVPose+ICP	61.3	93	51.2	78.8	53.4	82.3	<u>72.9</u>	75.8	71.1	
	PVN3D [S.6]	33.9	88.6	39.1	78.4	41.9	80.9	68.1	74.7	63.2	
	FFB6D [S.5]	-	-	-	-	-	-	-	-	66.2	
	PointVoteNet+ICP[S.4]	70.0	<u>95.5</u>	60.8	87.9	70.7	58.7	66.9	90.6	75.1	
3D/Mesh	RCVPose3D	63	96.1	57.3	81.4	54.2	81.5	75.1	80.7	73.7	
	RCVPose3D + ICP	<u>65.7</u>	96.4	<u>58.5</u>	<u>81.7</u>	<u>54.7</u>	<u>82</u>	75.4	<u>81.2</u>	<u>74.5</u>	

Table S.2. LMO accuracy results: accuracy of 6DoF PE methods for non-symmetric objects are evaluated with ADD, and that of symmetric objects (annotated with *) are evaluated with ADD-s.

Descriptors	ICP	Object								Mean
		ape	can	cat	driller	duck	eggbox*	glue*	hole-puncher	
PointNet++ [S.14]	✗	63	96.1	57.3	81.4	54.2	81.5	75.1	80.7	73.7
	✓	65.7	96.4	58.5	81.7	<u>54.7</u>	82	75.4	81.2	74.5
Point Transformer [S.23]	✗	59.2	93.4	56.8	80.8	58.2	79.6	73.2	85.4	73.3
	✓	<u>59.9</u>	<u>93.7</u>	<u>57.2</u>	<u>81.1</u>	58.6	<u>80.1</u>	73.6	<u>85.8</u>	<u>73.8</u>
PPF+knn	✗	55.7	88.6	51.2	78.2	54.1	79.4	73.8	85.7	70.8
	✓	56.8	89.4	51.6	78.8	54.8	80.2	<u>74.3</u>	87.2	71.7
FPFH+knn	✗	55.4	89.2	50.2	77.8	52.6	80.9	72.4	86.3	70.6
	✓	55.7	90.2	50.8	78.2	53.8	81.4	73.2	87.2	71.3
DGCNN[S.19]	✗	58	87.2	53.4	77.8	51.9	78.7	71.2	82.3	70.1
	✓	59.2	88.6	54.1	78.2	52.1	78.7	71.7	82.7	70.7
SubdivNet[S.8]	✗	42.3	83.2	49.2	77.8	48.7	77.9	69.2	75.2	65.4
	✓	45.2	83.7	49.7	78.2	49.2	78.2	70.1	75.2	66.2

Table S.3. LMO accuracy results for different descriptors: accuracy of RCVPose3D for non-symmetric objects is evaluated with ADD, and for symmetric objects (annotated with *) is evaluated with ADD-s.

Refine	Metric	Method	002 masker can	003 cracker box	004 sugar box	005 tomato soup can	006 mustard bottle	007 tuna fish can	008 pudding box	009 gelatin box	010 pointed meat can	011 banana	019 pitcher base	021 bleach cleanser	024 bowl*	025 mug	035 power drill	036 wood block*	037 scissors	040 large marker	051 large clamp*	052 extra large clamp*	061 foam block*	Mean		
No	ADD-S AUC	PoseCNN [S.21]	83.9	76.9	84.2	81.0	90.4	88.0	79.1	87.2	78.5	86.0	77.0	71.6	69.6	78.2	72.7	64.3	56.9	71.7	50.2	44.1	88.0	75.8		
		BaseNet [S.3]	95.4	93	98.5	96.5	97.7	97.7	97.7	97.3	97.3	99	95.7	97.7	97.9	97.4	97.7	97.8	97.7	91.3	98	77.4	66.4	98	94.4	
		DF(per-pixel)[S.18]	95.3	92.5	95.1	93.8	95.8	95.7	94.3	94.3	97.2	94.3	89.3	90.0	93.6	94.4	86.0	95.3	92.1	89.5	90.1	95.1	71.5	70.2	92.2	91.2
		PVN3D[S.6]	96.0	96.1	97.4	96.2	97.5	96	97.1	97.7	93.3	96.6	97.4	96.6	97.4	96.0	90.2	97.6	96.7	90.4	96.7	96.7	93.6	88.4	96.8	95.5
		FFB6D[S.5]	96.3	96.3	97.6	95.6	97.8	96.8	97.1	98.1	94.7	97.2	97.6	96.8	96.3	96.3	97.3	97.2	92.6	97.2	96.6	96.8	96.0	97.3	96.6	96.6
		RCVPose[S.20]	95.7	97.2	97.6	98.2	97.9	98.2	97.7	97.7	97.9	97.9	96.2	99.2	95.2	98.4	96.2	89.1	96.2	89.1	96.2	95.9	95.2	94.7	95.7	96.6
		RCVPose3D	92.1	96.9	97.4	96.9	97.6	96.7	97.7	97.8	97.7	97.8	98.2	98.4	98.6	92.2	98.6	97.1	93.2	97.7	96.7	92	93.4	95	96.3	96.3
		PoseCNN [S.21]	50.2	53.1	68.4	66.2	81.0	70.7	62.7	75.2	59.5	72.3	53.3	50.3	69.6	58.5	55.3	64.3	35.8	58.3	50.2	44.1	70.2	44.1	88.0	59.9
		DF(per-pixel)[S.18]	70.7	86.9	90.8	84.7	90.9	79.6	89.3	95.8	89.3	95.8	79.6	76.7	87.1	87.5	86.0	83.8	83.7	89.5	77.4	89.1	71.5	70.2	92.2	82.9
		PVN3D[S.6]	80.5	94.8	96.3	88.5	96.2	89.3	95.7	96.1	88.6	93.7	88.6	93.7	96.5	93.2	90.2	95.4	95.1	90.4	92.7	91.8	93.6	88.4	96.8	91.8
Yes	ADD(S) AUC	FFB6D[S.5]	80.6	94.6	96.6	89.6	97	88.9	94.6	96.9	88.1	94.9	96.9	94.8	96.3	94.2	95.9	92.6	90.6	95.7	89.1	96.8	96.0	97.3	92.7	
		BaseNet[S.3]	46.9	76.7	97.5	72.7	79.2	72	94.4	98.6	90.6	95.1	96.1	95.4	83.9	93.9	94.9	90	75.8	92.2	68.5	25.3	92.9	82.5	82.5	
		RCVPose	93.6	95.7	97.2	94.7	97.2	96.4	97.1	96.5	90.2	96.7	95.7	97.8	97.8	95.2	96.3	95.4	89.1	94.7	92.4	95.2	94.7	95.7	95.2	
		RCVPose3D	91.7	96.2	95.4	94.3	95.6	96.2	96.7	97	98.2	97.9	98.2	97.7	98.2	92.2	98.6	96.7	93.2	97.2	96.4	92	93.4	95	95.7	
		PoseCNN [S.21]+ICP	95.8	92.7	98.2	94.5	98.6	97.1	97.9	98.8	92.7	97.1	97.8	96.9	96.9	81.0	94.9	98.2	87.6	91.7	97.2	75.2	64.4	97.2	93.0	
		DF(Iterative)[S.18]	96.4	95.8	97.6	94.5	97.3	97.1	96.0	98.0	90.7	96.2	97.5	95.9	95.9	89.5	96.7	96.0	92.8	92.0	97.6	72.5	69.9	92.0	93.2	
		PVN3D[S.6]+ICP	95.2	94.4	97.9	95.9	98.3	96.7	98.2	98.8	93.8	98.2	97.6	97.2	97.6	92.8	97.7	97.1	91.1	95.0	98.1	95.6	90.5	98.2	96.1	
		RCVPose+ICP	96.2	97.9	97.9	99	98.2	98.6	98.1	98.4	98.4	98.3	97.2	98.3	97.2	99.6	96.9	98.7	96.4	90.7	96.4	96.6	96.2	95.1	96.6	97.2
		RCVPose3D	92.4	97.2	97.7	97.2	97.9	97	98	98	99	98.5	98.7	98.8	97.4	98.6	97.4	93.7	97.4	93.7	97.9	97	92.3	93.7	95.2	96.6
		PoseCNN [S.21]+ICP	68.1	83.4	97.1	81.8	98.0	83.9	96.6	98.1	83.5	91.9	96.9	92.5	81.0	81.1	97.7	87.6	78.4	85.3	75.2	64.4	97.2	85.4		
ADD(S) AUC	DF(Iterative)[S.18]	73.2	94.1	96.5	85.5	94.7	81.9	93.3	96.7	83.6	83.3	96.9	89.9	89.5	88.9	92.7	92.8	77.9	93.0	72.5	69.9	92.0	86.1			
	PVN3D[S.6]+ICP	79.3	91.5	96.9	89.0	97.9	90.7	97.1	98.3	87.9	96.0	96.9	95.9	92.8	96.0	95.7	91.1	87.2	91.6	95.6	90.5	98.2	92.3			
	RCVPose+ICP	94.7	96.4	97.6	95.4	97.1	96.7	97.4	97.9	92.6	97.2	96.7	98.4	95.3	97.1	96.9	90.7	94.9	93.2	96.2	95.1	96.6	95.9			
	RCVPose3D	92	96.8	95.6	94.6	95.9	96.4	97	97.3	98.4	98.2	98	98.4	92.5	98.8	97	93.7	93.7	97.2	96.7	92.3	93.7	95.2	96.0		

Table S.4. YCB accuracy results: AUC [S.21] and ADD(S) [S.7] are used as follows: 6DoF PE methods are evaluated with ADD for non-symmetric objects, and are evaluated with ADD-S for symmetric objects (annotated with *) while computing for ADD(S) AUC.

Refine	Metric	Method	002 master can	003 cracker box	004 sugar box	005 tomato soup can	006 mustard bottle	007 tuna fish can	008 pudding box	009 gelatin box	010 potato can	011 banana	019 pitcher	021 bleach	024 bowl*	025 mug	035 power drill	036 wood block*	037 scissors	040 large marker	051 large clamp*	052 extra large clamp*	061 togn brick*	Mean		
No	ADD-S AUC	PointNet++ [S.14]	92.1	96.9	97.4	96.9	97.6	96.7	97.7	97.8	98.7	98.2	98.4	98.6	92.2	98.6	97.1	93.2	97.7	96.7	92	93.4	95	96.3		
		PPF+knn	92.3	96.2	97.6	97.7	93.2	97.7	93.2	97.6	96.9	97.9	97.4	97.7	98.2	92.2	97.7	96.9	93.2	96.7	93.2	92.3	93.2	94.7	95.5	
		FPPH+knn	90.2	95.6	95.1	91.7	94.9	94.3	95.7	97.2	96.2	97.1	96.2	97.1	96.2	97.7	87.9	97.3	96.1	93.5	96	96.9	91.2	92.2	93.4	94.6
		DGCNN [S.19]	87.2	94.7	95.2	93.7	90.4	94.5	93.2	96.7	93.2	96	95.1	93.2	84.3	94.2	95.4	91.2	95.1	94.2	89.6	90.9	91.1	91.1	92.8	
		SubdivNet [S.8]	89.1	92.6	93.3	90.2	91.2	92.1	94.1	95.9	93.6	96.3	92.4	91.7	83.8	94.4	93.7	91.4	93.4	91.7	90	88.7	91.4	91.4	92.0	
	ADD(S) AUC	PointNet++ [S.14]	91.7	96.2	95.4	94.3	95.6	96.2	96.2	97.7	97.9	98.2	97.9	97.7	98.2	92.2	98.6	96.7	93.2	97.2	96.4	92	93.4	95	95.7	
		PPF+knn	91.7	95.9	93.4	92.8	94.3	95.1	95.3	95.4	97.1	96.4	96.2	97.4	92.2	98.6	96.1	93.2	97	95.7	92.3	93.2	94.7	95.0		
		FPPH+knn	88.7	94.8	93.7	89.6	93.2	92.3	94.3	95.6	94.4	95.1	93.6	96.1	87.9	95.7	93.1	93.5	94.3	95.2	91.2	92.2	93.4	93.2		
		DGCNN [S.19]	86.9	93.2	91.7	90.2	88.6	94.2	91.7	93.3	90.1	94.2	91.5	90.7	80.2	92.7	92.6	88.7	92.3	93.7	89.6	90.9	91.1	90.9		
		SubdivNet [S.8]	88.8	91.4	90	89.4	90.2	91.3	92.4	94.1	91.2	93.9	91.1	88.6	80	93.1	91.5	89.2	91.7	90.9	90	88.7	91.4	91.4	90.4	
Yes	ADD-S AUC	PointNet++ [S.14]	92.4	97.2	97.7	97.2	97.9	97	98	98	98.5	98.7	98.8	92.4	98.6	97.4	97.9	97.2	93.5	97	93.4	92.6	93.5	95	95.8	
		PPF+knn	92.6	96.4	98.2	93.9	98	93.9	97.9	97.1	98.2	97.6	97.9	98.6	92.4	97.9	97.2	93.5	97	93.4	92.6	93.5	95	95.8		
		FPPH+knn	90.5	96	95.6	92	95.2	94.7	95.9	97.4	96.5	97.3	96.5	97.9	87.9	97.5	96.4	93.9	96.4	97.1	91.4	93.5	93.7	94.9		
		DGCNN [S.19]	87.5	95	95.4	94	90.6	94.7	93.5	96.9	93.4	96.3	95.4	93.5	84.3	94.4	95.7	91.2	95.3	94.4	89.8	91.1	91.3	93.0		
		SubdivNet [S.8]	89.3	92.9	93.5	90.4	91.5	92.4	94.4	96.1	93.9	96.5	92.6	92	83.8	94.7	94	91.4	93.6	92	90.2	89	91.6	92.2		
	ADD(S) AUC	PointNet++ [S.14]	92	96.8	95.6	94.6	95.9	96.4	97	97.3	98.4	98.2	98	98.4	92.5	98.8	97	93.7	97.2	96.7	92.3	93.7	95.2	96.0		
		PPF+knn	92	96.2	93.7	93.1	94.5	95.4	95.9	95.6	97.3	96.6	96.4	97.6	92.4	98.9	96.4	93.5	97.1	96	92.6	93.5	95	95.2		
		FPPH+knn	89	95.3	94.1	90.1	93.5	94.7	95.9	94.7	93.8	96.4	87.9	96.1	93.3	93.9	95	95.5	91.4	93.5	93.7	93.6				
		DGCNN [S.19]	87.2	93.4	92	90.4	88.9	94.5	92	93.5	90.4	94.4	91.8	90.9	80.2	92.7	92.9	88.7	92.5	94	89.8	91.1	91.3	91.1		
		SubdivNet [S.8]	89.1	91.6	90.2	89.7	90.4	91.6	92.6	94.4	91.5	94.2	91.4	88.8	80	93.3	91.8	89.2	91.9	91.1	90.2	89	91.6	90.6		

Table S.5. YCB ADD-S AUC [S.21] and ADD(S) AUC [S.7] results with different descriptors: Non-symmetric objects are evaluated with ADD, and symmetric objects (annotated with *) are evaluated with ADD-S for ADD(S) AUC. The ADD-S AUC metrics is based on the curve with ADD-S for both non-symmetries and symmetries.

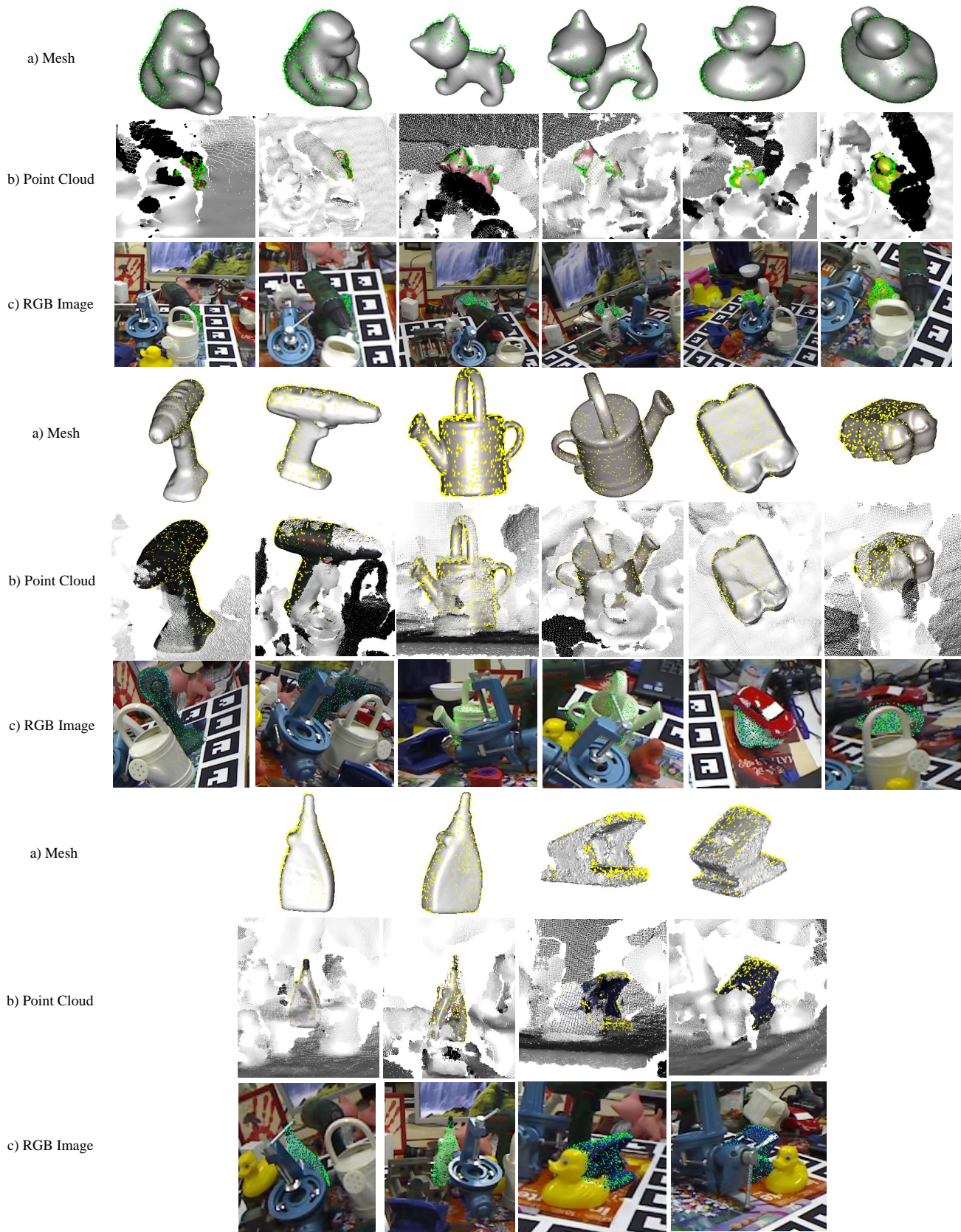


Figure S.1. More Samples of RCVPose3D results on Occlusion LINEMOD: The meshes are applied with groundtruth (GT) pose, the green points are applied with estimated poses, whereas the blue dots are projected GT poses. The color in Point Cloud and RGB images are for illustration only, as RGB data is not used for training or inference

References

- [S.1] Haowen Deng, Tolga Birdal, and Slobodan Ilic. Ppfnet: Global context aware local features for robust 3d point matching. In *Proceedings of the IEEE conference on computer vision and pattern recognition*, pages 195–205, 2018. 2
- [S.2] Bertram Drost, Markus Ulrich, Nassir Navab, and Slobodan Ilic. Model globally, match locally: Efficient and robust 3d object recognition. In *2010 IEEE computer society conference on computer vision and pattern recognition*, pages 998–1005. Ieee, 2010. 2
- [S.3] Ge Gao, Mikko Lauri, Yulong Wang, Xiaolin Hu, Jianwei Zhang, and Simone Frntrop. 6d object pose regression via supervised learning on point clouds. In *2020 IEEE International Conference on Robotics and Automation (ICRA)*, pages 3643–3649. IEEE, 2020. 4
- [S.4] Frederik Hagelskjær and Anders Glent Buch. Pointvotenet: Accurate object detection and 6 dof pose estimation in point clouds. In *2020 IEEE International Conference on Image Processing (ICIP)*, pages 2641–2645. IEEE, 2020. 3
- [S.5] Yisheng He, Haibin Huang, Haoqiang Fan, Qifeng Chen, and Jian Sun. Ffb6d: A full flow bidirectional fusion network for 6d pose estimation. In *Proceedings of the IEEE/CVF Conference on Computer Vision and Pattern Recognition*, pages 3003–3013, 2021. 3, 4
- [S.6] Yisheng He, Wei Sun, Haibin Huang, Jianran Liu, Haoqiang Fan, and Jian Sun. Pvn3d: A deep point-wise 3d keypoints voting network for 6dof pose estimation. In *Proceedings of the IEEE/CVF Conference on Computer Vision and Pattern Recognition (CVPR)*, June 2020. 3, 4
- [S.7] Stefan Hinterstoisser, Vincent Lepetit, Slobodan Ilic, Stefan Holzer, Gary Bradski, Kurt Konolige, and Nassir Navab. Model based training, detection and pose estimation of texture-less 3d objects in heavily cluttered scenes. In *Asian conference on computer vision*, pages 548–562. Springer, 2012. 4, 5
- [S.8] Shi-Min Hu, Zheng-Ning Liu, Meng-Hao Guo, Jun-Xiong Cai, Jiahui Huang, Tai-Jiang Mu, and Ralph R Martin. Subdivision-based mesh convolution networks. *arXiv preprint arXiv:2106.02285*, 2021. 1, 2, 3, 5
- [S.9] Yinlin Hu, Joachim Hugonot, Pascal Fua, and Mathieu Salzmann. Segmentation-driven 6d object pose estimation. In *Proceedings of the IEEE/CVF Conference on Computer Vision and Pattern Recognition*, pages 3385–3394, 2019. 3
- [S.10] Wadim Kehl, Fabian Manhardt, Federico Tombari, Slobodan Ilic, and Nassir Navab. Ssd-6d: Making rgb-based 3d detection and 6d pose estimation great again. In *Proceedings of the IEEE international conference on computer vision*, pages 1521–1529, 2017. 3
- [S.11] Markus Oberweger, Mahdi Rad, and Vincent Lepetit. Making deep heatmaps robust to partial occlusions for 3d object pose estimation. In *Proceedings of the European Conference on Computer Vision (ECCV)*, pages 119–134, 2018. 3
- [S.12] Kiru Park, Timothy Patten, and Markus Vincze. Pix2pose: Pixel-wise coordinate regression of objects for 6d pose estimation. In *Proceedings of the IEEE/CVF International Conference on Computer Vision*, pages 7668–7677, 2019. 3
- [S.13] Sida Peng, Yuan Liu, Qixing Huang, Xiaowei Zhou, and Hujun Bao. Pvnnet: Pixel-wise voting network for 6dof pose estimation. In *Proceedings of the IEEE/CVF Conference on Computer Vision and Pattern Recognition*, pages 4561–4570, 2019. 3
- [S.14] Charles R Qi, Li Yi, Hao Su, and Leonidas J Guibas. Pointnet++: Deep hierarchical feature learning on point sets in a metric space. *arXiv preprint arXiv:1706.02413*, 2017. 1, 2, 3, 5
- [S.15] Radu Bogdan Rusu, Nico Blodow, and Michael Beetz. Fast point feature histograms (fpfh) for 3d registration. In *2009 IEEE international conference on robotics and automation*, pages 3212–3217. IEEE, 2009. 2
- [S.16] Bugra Tekin, Sudipta N Sinha, and Pascal Fua. Real-time seamless single shot 6d object pose prediction. In *Proceedings of the IEEE Conference on Computer Vision and Pattern Recognition*, pages 292–301, 2018. 3
- [S.17] Ameni Trabelsi, Mohamed Chaabane, Nathaniel Blanchard, and Ross Beveridge. A pose proposal and refinement network for better 6d object pose estimation. In *Proceedings of the IEEE/CVF Winter Conference on Applications of Computer Vision*, pages 2382–2391, 2021. 3
- [S.18] Chen Wang, Danfei Xu, Yuke Zhu, Roberto Martín-Martín, Cewu Lu, Li Fei-Fei, and Silvio Savarese. Densefusion: 6d object pose estimation by iterative dense fusion. In *Proceedings of the IEEE/CVF Conference on Computer Vision and Pattern Recognition*, pages 3343–3352, 2019. 4
- [S.19] Yue Wang, Yongbin Sun, Ziwei Liu, Sanjay E Sarma, Michael M Bronstein, and Justin M Solomon. Dynamic graph cnn for learning on point clouds. *Acm Transactions On Graphics (tog)*, 38(5):1–12, 2019. 1, 2, 3, 5
- [S.20] Yangzheng Wu, Mohsen Zand, Ali Etamad, and Michael Greenspan. Vote from the center: 6 dof pose estimation in rgb-d images by radial keypoint voting. *arXiv preprint arXiv:2104.02527*, 2021. 4
- [S.21] Yu Xiang, Tanner Schmidt, Venkatraman Narayanan, and Dieter Fox. Posecnn: A convolutional neural network for 6d object pose estimation in cluttered scenes. 2018. 3, 4, 5
- [S.22] Sergey Zakharov, Ivan Shugurov, and Slobodan Ilic. Dpod: 6d pose object detector and refiner. In *Proceedings of the IEEE/CVF International Conference on Computer Vision*, pages 1941–1950, 2019. 3
- [S.23] Hengshuang Zhao, Li Jiang, Jiaya Jia, Philip HS Torr, and Vladlen Koltun. Point transformer. In *Proceedings of the IEEE/CVF International Conference on Computer Vision*, pages 16259–16268, 2021. 1, 2, 3